Research Square

Preprints are preliminary reports that have not undergone peer review.
They should not be considered conclusive, used to inform clinical practice,
or referenced by the media as validated information.

Simulated thermal rheology of pork adipose tissues by glycerolysis palm olein and pea protein fibril emulsion gels

Bingjie Hu
Jinan University
Ke Dang
Jinan University
Yee Ying Lee
Monash University Malaysia
Hui Liao
Jinan University
Chin-Ping Tan
Universiti Putra Malaysia
Meng Zhang
Jinan University
Yong Wang
Jinan University
Chaoying Qiu
tcyqiu@jnu.edu.cn
Jinan University

Article

Keywords: pork adipose tissue, adipose tissue mimetics, pea protein fibrils, structured lipids, heating stability

Posted Date: March 5th, 2026

DOI: https://doi.org/10.21203/rs.3.rs-8868920/v1

License: This work is licensed under a Creative Commons Attribution 4.0 International License.
Read Full License

Additional Declarations: No competing interests reported.

Abstract

The demand for plant-based meat analogues as healthier and sustainable dietary choices continues to rise. However, current fat replacers face challenges in fully simulating the unique thermal behavior of natural animal fat. This study investigated the application of pea protein fibril (PPF), sodium alginate (SA) complexes and enzymatically glycerolized palm olein in the preparation of adipose tissue mimetics, with a focus on their thermo-rheology stability. The PPF-SA complexes are formed through electrostatic, hydrophobic, and hydrogen-bond interactions, exhibiting superior interfacial activity and an increased degradation temperature. These composites coexist around the droplets within a cross-linked network, simulating the tightly packed droplet structure of porcine adipose tissue. At an oil/water ratio of 4:6 and a Ca^{2+} concentration of 100 mM, the emulsion gel exhibits a robust cross-linked network, and enhanced thermal stability. Furthermore, a higher monoacylglycerol (MAG) content in the glycolysis lipids reduced the interfacial tension and improve emulsion stability, imparting enhanced heating and freeze-thawing stability. This study provides a novel strategy utilizing colloidal interactions, crystal/polymer network formation and structured lipid selection to define the texture and functionality of adipose tissue mimetics with the slow-rendering melting attributes of animal fat.

1. Introduction

Animal fat serves as an essential energy source and provides a multi-sensory flavor and texture experience of flavor and texture, owning to its unique structure and thermal-phase transition behavior[1]. However, global animal fat consumption is exacerbating environmental pressures related to carbon emissions, land use, and ecological sustainability. Moreover, excessive intake of saturated fat is closely linked to elevated rates of obesity, type 2 diabetes, and cardiovascular diseases, posing significant public health risks[2]. Driven by these concerns, there is a rapidly growing demand plant-based fat analogues that reduce energy intake and minimize saturated or trans fatty acids.

The intracellular fats in pork adipose tissue consisting of adipocytes filled with solid lipids and surrounded by collagenous connective tissue form the key structural basis for their texture behaviors, temperature-dependent functionality and juicy mouthfeel. Currently, plant lipid substitutions such as coconut and palm oil, along with various lipid modification approaches, are being explored. Among these, enzymatic glycerolysis has gained attention for its ability to restructure the glycerol backbone of lipids without altering fatty acid composition, thereby enabling a higher solid fat content and a melting profile closer to that of pork fat[3]. Palm olein (PO) is a sustainable tropical oil frequently utilized for its balanced unsaturated/saturated fatty acids ratio and high oxidative stability. Through glycerolysis, the solid fat content and melting point can be remarkably increased due to the generation of monoacylglycerols (MAG) and diacylglycerols (DAG), which possess higher crystallization temperatures and health benefits, making them promising alternatives to triacylglycerol lipids[4]. MAG/DAG can also form interfacial-active lipid crystals and rigid shells, imparting unique gelation and stabilization effects[5]. However, while fat substitute strategies utilizing mono/mixed component oleogels and biphasic

emulsion gels with partial acylglycerols, or waxes have been explored, many current models either melt rapidly at high temperatures due to structural collapse or remain excessively rigid during cooking, presenting significant challenges for practical application[6,7].

To reduce dependence on lipid crystals and enhance network rigidity, composite fat replacers featuring enhanced interfacial assembly or cross-linking via plant proteins and polysaccharides have been developed[8]. However, single network polysaccharide gels fall short of replicating the complex connective tissue network of animal fats or achieving the structural integrity with slow melting performance during heating process (e.g., frying, roasting, or baking)[9–11]. Protein amyloid fibrils characterized by a high aspect ratio and a multitude of functional groups are excellent stabilizers for emulsion gels and have been utilized to reinforce hydrogels matrices[12]. Pea protein amyloid fibrils can enhance gel rigidity through intensified intermolecular interactions when combined with sodium alginate (SA). This combination forms the classic "egg-box" structure upon the addition of Ca^{2+} creating a robust cross-linked crystalline/polymeric network. Moreover, our recent study revealed that amyloid fibrils can mediate DAG crystallization and promoting the ordered alignment of crystals at the droplet interface and further enhancing emulsion gel strength. This provides a viable pathway to improve emulsion performance and simulate the thermal-rheological properties of animal fat.

Consequently, this study proposes a strategy for plant-based adipose tissue mimetics by constructing a composite emulsion gel using pea protein fibrils and SA, with glycerolized palm olein (PO) serving as the intracellular fat. The complexation mechanisms of PPF-SA and their influence on the resulting emulsion gels were characterized. Furthermore, the effect of the MAG/DAG ratio in the glycerolized PO was systematically explored by evaluating interfacial properties and thermo-rheological profiles. The synergistic effects between the glycerolized lipids and the SA-fibrils complex on the matrix's properties are illustrated. This study provides critical insights into fabricating adipose tissue mimetics, offering a promising framework for developing animal fat analogues with comparable softening behavior during cooking for applications in plant-based burgers and sausages.

2. Results

2.1 Physicochemical properties of protein-SA complex

2.1.1 Turbidity, morphology and zeta-potential of complex

Turbidity and TEM analysis illustrate the aggregation states of the complexes. As shown in Fig. 1A and B, the PPI solution exhibited a turbidity of 0.37 and contained aggregates composed of spherical or rod-shaped particles. In contrast, the PPF solution showed a lower turbidity of 0.18 and contained numerous semi-flexible fibrils with high aspect ratios, some of which were stacked into form fibrous aggregates. This is attributed to the formation of nanoscale PPF through acid hydrolysis and peptide self-assembly, resulting in a smaller particle size and higher dispersibility, which reduces light scattering[13]. With an

increasing SA ratio, the turbidity of the PPI-SA complexes decreased from 0.36 to 0.21, accompanied by a gradual reduction in the degree of aggregation as visualized by TEM. This indicates that SA weakened PPI aggregation by attenuating the attractive interactions between protein molecules[14]. In contrast, the turbidity of the PPF-SA complexes slightly increased from 0.18 to 0.26 with an increasing SA ratio. TEM images (Fig. 1B) showed that the PPF-SA complexes were entangled, accounting for a higher aggregation and the increased size of the composite aggregates[15] A similar phenomenon has been reported for whey protein-SA complexes where dense complexes was observed[16]. In this case, the addition of the polysaccharides allowed the fibrils to be linked via the alginate chains, promoting the formation of larger aggregates.

The surface charge of the complexes serves as a critical indicator for evaluating electrostatic interactions. As shown in Fig. 1C, the absolute zeta-potential of PPI (–21.39 mV) was markedly higher than that of PPF (–12.97 mV). This difference is attributed to the exposure of more $–NH_3^+$ terminal groups in the PPF during hydrolysis. At pH 7 these groups undergo protonation, leading to a lower net negative surface charge. SA, as a natural anionic polysaccharide, contains abundant α-L-guluronate (G) and β-D-mannuronate residues with a zeta-potential of − 65.50 mV[16]. The zeta-potential of both PPI-SA and PPF-SA complexes decreased significantly upon the addition of SA, confirming adsorption via electrostatic interactions[17]. Notably, despite PPI having a higher initial zeta-potential than PPF, the PPI–SA complex exhibited a more significant charged reduction. This suggests that PPF exposes more short peptide fragments containing $–NH_3^+$ groups, providing more positive binding sites and stronger electrostatic forces, thereby enhancing SA adsorption[18].

2.1.2 Interfacial tension of protein-SA complex

To investigate the potential of these complexes to stabilize the oil-water interface, their interfacial tension was monitored over time. As shown in Fig. 1D. all the samples exhibited a decrease in interfacial tension within the first 200 s, indicating rapid migration to the interface. Subsequently, the rate of reduction slowed, suggesting that the complexes underwent reorientation and rearrangement until an equilibrium state was achieved at 3500 s[19]. PPI and PPF exhibited equilibrium interfacial tensions of 5.39 mN/m and 4.98 mN/m, respectively, demonstrating high interfacial activity. The flexible nanoscale fibrillar structure of PPF confers a high specific surface area and surface hydrophobicity, enabling faster adsorption at the interface compared to native PPI[20]. Following complexation with SA, the interfacial tension was further reduced. This improvement is attributed to a synergistic adsorption effect, in which SA promotes the spreading and stabilization of the complexes at the interface[21]. In addition, the high aspect ratio structure of the PPF-SA complex allowed for the formation of bridging structures at the interface providing higher surface activity[22]. Notably, the interfacial tension of the PPF-SA complex remained consistently lower than that of PPI-SA, reaching a minimum value at a mass ratio of 10:3. This suggests that the formation of the complex reduced the spatial steric hindrance typically associated with interfacial adsorption. Concurrently, the flexible chains of SA may have facilitated more facile spreading at the interface enabling the formation of multiple anchoring points, and ultimately lowering

the interfacial tension[23,24]. However, when the SA ratio was further increased to 4:9, the interfacial tension rose, likely due to the excessive adsorption of SA which may have hindered efficient packing at the interface.

2.1.3 Thermal stability of protein-SA complex

Thermogravimetric (TG) and derivative thermogravimetry (DTG) analysis were employed to systematically evaluate the thermal stability of the complexes. As shown in Fig. 1E, all samples exhibited similar three-stage thermal degradation. The first stage occurred between 30–150°C, where weight loss was attributed to the evaporation of absorbed and loosely bound water[25]. The significant weight loss between 200–500°C represented the major stage of thermal degradation involving the pyrolysis/volatilization of oxygen-containing groups such as hydroxyl and carboxyl groups and other side chains in the polysaccharide or protein complexes, as well as the thermal disintegration of intermolecular hydrogen bonds[26]. The third stage occurred between 500°C–600°C, and was characterized by a gradual decrease in mass, attributed to the further degradation of carbonaceous residues.

During the main degradation stage (200–500°C), $T_{50\%}$ (the temperature at which mass loss reaches 50%) and DTG_{max} (the temperature of the maximum rate of mass loss) were used to evaluate thermal stability in detail. SA showed a lower $T_{50\%}$ and DTG_{max} than PPI and PPF, indicating lower thermal stability. PPI exhibited a higher $T_{50\%}$ (414°C) than PPF (405°C), while both showed similar DTG_{max} (324°C and 325°C) values. This suggests that PPI formed larger denser aggregates than nanoscale PPF, providing higher resistance to initial thermal decomposition. Notably, the $T_{50\%}$ and DTG_{max} of the PPF-SA complex were consistently higher than those of the PPI-SA complexes at all corresponding SA ratios, indicating that the PPF-SA complex possesses superior thermal stability. This enhancement likely originates from stronger intermolecular interactions between the PPF and SA[27]. However, an increase in SA ratio led to a general decrease in $T_{50\%}$ and DTG_{max} reflecting the influence of the polysaccharide's inherently lower thermal decomposition threshold on the overall complex.

2.2 Molecular interactions of protein-SA complex

2.2.1 Intrinsic fluorescence and FT-IR of protein-SA complex

Intrinsic fluorescence, primarily from tryptophan, phenylalanine, and tyrosine are residues, is highly sensitive to the surrounding microenvironments and can be monitored to assess protein conformational changes. As shown in Fig. 2A, the initial fluorescence intensities for PPI and PPF were 6998 a.u. and 6052 a.u., respectively. Upon complexation with SA (12:1 and 10:3), intensities increased to 8419 a.u. and 7936 a.u. for PPI-SA, and 6796 a.u. and 6587 a.u. for PPF-SA, respectively. Aromatic amino acids typically exhibit higher quantum yields in hydrophobic environments[28]. Therefore, the increased in fluorescence intensity likely stem from SA binding to positively charged regions on the protein surface, which enhances hydrophobic interactions and promotes the exposure of internal Trp residues[29].

However, at an SA ratio of 4:9. the intensity decreased to 6903 a.u. and 6061 a.u, respectively. This reduction is due to the excessive SA adhering to the PPI/PPF surface, which effectively conceals aromatic amino acids[30]. Figure 3A further shows that increasing Ca^{2+} concentration does not alter the peak position or relative intensity, indicating that the microenvironment of the aromatic amino acids remains essentially unchanged, and the protein secondary structure is preserved. These findings support a mechanism where Ca^{2+} preferentially coordinates with carboxylate sites in the guluronic acid block (G-blocks), forming an “egg-box” cross-linking structure without interacting with the aromatic side chains of the protein[31].

FT-IR results are presented in Fig. 2B. The amide I band (C = O stretching) reflects changes in secondary structure. The main peak for PPI in the amide I band was observed at ~ 1654 cm^{-1}, whereas for PPF it shifted slightly lower to ~ 1651 cm^{-1}, indicating an increasing in β-sheet structures following fibrillation[32]. The amide A band (3000–3500 cm^{-1}) corresponds to O–H bending vibrations and N–H stretching vibrations, characteristic of hydrogen bonding. After fibrillation, this peak shifted from 3386 cm^{-1} to a lower wavenumber 3288 cm^{-1}, suggesting that PPF possesses stronger hydrogen bond interactions, as the formation of abundant, hydrogen-bond-stabilized β-sheet structures is a hallmark of amyloid fibrils[33]. The characteristic peaks of SA appeared at 1609 cm^{-1}, corresponding to the asymmetric and symmetric stretching of carboxylate anions (COO^-). As the SA ratio increased, the amide A band shifted toward a lower wavenumber because of the hydrogen bond interactions between SA and the O–H/N–H groups on the proteins/protein fibril (Zhu et al., 2025). Finally, the amide I peaks of PPI/PPF gradually shifted toward the characteristic peaks of pure SA, confirming that the PPI/PPF-SA interaction is driven by hydrogen bonding and physical entanglement[34].

Upon the addition of Ca^{2+}, the peak in the amide I region of SA shifted from 1609 cm^{-1} to 1617 cm^{-1}. These spectral changes demonstrate a pronounced ionic cross-linking effect between Ca^{2+} and the carboxylate groups ($–COO^-$) of SA[35]. Multiple adjacent carboxylate groups assembled into a stable, ionically cross-linked network mediated by Ca^{2+} forming the characteristic “egg-box” structure. In addition, the O–H/N–H stretching vibration peak in the amide A region shifted from 3397 cm^{-1} to 3443 cm^{-1}. This change reflects the reorganization of the hydrogen bonding network within the structure, specifically, the transition toward high wavenumbers suggests a change in the environment of the hydroxyl and amino groups as the ionic network forms[36]. Both the PPI–SA and PPF–SA composite systems exhibited similar spectral shifts in the amide I and amide A regions, indicating that Ca^{2+} preferentially cross-links with SA and governs the overall formation of the gel network. In summary, PPI/PPF primarily associate with SA through hydrogen bonding to form non-covalent complexes. Following the addition of Ca^{2+}, the ions coordinate with the carboxylate groups of SA to establish a three-dimensional “egg-box” linked matrix which serves as the structural framework for the composite gel.

2.2.2 Thioflavin T (ThT) fluorescence and surface hydrophobicity (H_0)

Thioflavin T (ThT) fluorescence is generally correlated with the presence of ordered β-sheets and is used to characterize amyloid fibril structures. As shown in Fig. 2C, the ThT fluorescence intensity of PPF was significantly higher than that of PPI ($p < 0.05$). This is attributed to the proteolysis and self-assembly of the protein into amyloid-like fibrils rich in β-sheet structures[37]. Upon complexation with SA, the ThT fluorescence intensity decreased markedly for both PPI and PPF. However, the ThT fluorescence intensity did not decrease further with increasing SA ratio.This suggests that the number of available binding sites between ThT and PPI/PPF was reduced due to the coverage of SA. Rather than disrupting the core cross-β scaffold of the fibrils, SA likely reduces ThT binding accessibility by modulating the surface charge and introducing steric hindrance[22]. Similar observations have been reported for protein fibrils complexed with chitosan, where the polysaccharide promotes the aggregation of the complexes thereby reducing ThT fluorescence intensity[38].

H_0 reflects the hydrophobicity interactions of proteins within their complexes. As shown in Fig. 2D, in the absence of SA, the H_0 of PPF was significantly higher than that of PPI ($P < 0.05$). This indicates that the fibrillation process disrupts the compact globular conformation of PPI, exposing hydrophobic residues that were originally buried[39]. Following complexation with SA, the H_0 decreased, suggesting that SA covers the hydrophobic regions on the protein surface via hydrophobic interactions, effectively shielding these sites[40]. Notably, although the initial the H_0 of the PPF–SA complex was lower than that of the PPI–SA complex. This indicates that PPF, with its high hydrophobicity and extended one-dimensional fibrillar structure, provides a more extensive and continuous hydrophobic binding interface for SA molecules. Stronger hydrophobic interactions allow SA to more effectively embed and shield the hydrophobic groups on the PPF. Overall, the formation of the PPF-SA complex is driven by a synergistic combination of hydrogen bonding, hydrophobic interactions, and electrostatic interaction.

2.3 Structure and temperature sweep of adipose tissue mimetics

2.3.1 Influence of PPF/SA ratio

As shown in Fig. 3A, the pork adipose tissue exhibited a typical white color, a smooth surface, and a three-dimensional block-like morphology. Both the PPI-SA and PPF-SA mimetics presented as white block structures with no significant free oil droplets or oil exudation, indicating that a high degree of visual similarity to natural pork adipose tissue. The microstructure of the mimetics was further characterized using SEM. At PPI:SA = 12:1 and 10:3, the mimetics exhibited pronounced shrinkage and collapse despite their block-like morphology appearance, this is likely attributable to volume contraction and localized collapse of the globular protein gel matrix[41]. At a PPI:SA = 4:9, an increase in laminated structures was noted, indicating a greater tendency to form a continuous matrix cross-linked by SA[42]. In contrast, the PPF-SA mimetics (at PPF:SA = 12:1 and 10:3), featured numerous spherical droplets structures enveloped by a continuous interpenetrating gel matrix. This suggests a sequential gelation mechanism the protein fibrils first form a flexible network, after which Ca^{2+} ion slowly diffuse through

the network gaps, to cross-link with SA, creating a second rigid network layer. This results in a composite "droplet-filled and crosslinked network" structure. This formation likely stems from the high interfacial activity of PPF-SA complex, which improves adsorption capacity and stabilizes the droplet[43]. Conversely, in the PPI-SA system, unencapsulated and discrete structured lipids hindered carboxylate cross-linking, thereby impairing the continuity of the gel matrix. Similar research indicates that an uneven distribution of the structured lipids characterized by heterogeneity droplet sizes reduces network continuity and introduces larger pores or weak regions, compromising the overall integrity of the gel structure[44]. These findings suggest that PPF-SA effectively improves the system's microstructure, plays a critical role in network formation.

Temperature-sweep tests were conducted to systematically investigate the evolution of the G' (storage modulus) and tan δ (the loss factor parameter) relative to temperature (Fig. 3B and 3C). The glycerolized PO exhibited higher melting point indicating a greatly enhanced solid fat content in lipid phase (Table. S1), making suitable for the fabrication of adipose tissue mimetics. The high G' at low temperatures results from the lipid molecular building blocks self-assembling into a three-dimensional crystal network within a complex hierarchical structure, providing firmness/elasticity at room temperature and tenderness at oral temperatures.

For natural pork adipose tissue, a reversible trend of "softening upon heating and hardening upon cooling" was observed driving by the melting and crystallization of the solid fat. Notably, at 4°C, pork fat exhibited a high G' of approximately 10^6 Pa, this indicating that the high concentration saturated fatty acids (42.36%, Table. S1) supports the texture before heating. At 80°C, even as the temperature far exceeded the melting point of the fat, the sample continued to exhibit predominantly elastic behavior. This indicates that the protein network continues to dominate the overall elastic response[45]. Upon cooling, the tissue regains its original stiffness demonstrating its ability to retain molten fat an essential factor for texture, palatability, and consumer acceptance. The mimetics (both PPI–SA and PPF–SA) exhibited G G' value of approximately ~ 10^5 which were lower (softer) than those of natural natural pork adipose tissue. G' significantly decreased between 4–40°C, indicating the progressive melting of the structured lipid crystals[46]. Upon further heating to 80°C, distinct differences emerged the PPI-SA samples showed a more pronounced attenuation of G' (dropping to 100–1000 Pa) and while the PPF-SA samples maintained a high and stablec between 1000 Pa and 10,000 Pa. Similar studies have also shown that the addition of 0.5% of SA is beneficial for maintaining thermal stability at elevated temperatures[47] This suggests a structural transition in the gel, where the mechanical strength shifts from being dominated by a droplet-structured lipid network to a continuous cross-linked network. Consequently, PPF maintains structural integrity more effectively than PPI, making it a superior candidate for mimicking the extracellular matrix of animal adipose tissue. In the PPF-SA system, the Ca^{2+} induced “egg-box” network serves as a robust supporting framework that maintains structural integrity at high-temperatures, effectively mimicking the extracellular matrix of animal adipose tissue[48].

Analysis of tan δ further clarifies the thermal response. As shown in Fig. 3C, as temperatures rose from 5 to 30°C, the tan δ of pork adipose tissue increased from 0.20 to 0.52, indicating that most of the lipid had transitioned from a highly elastic response to a predominantly viscous response[45]. Notably, for PPI–SA, tan δ increased markedly (exceeding 0.60), whereas PPF–SA it only reached approximately 0.40. These results suggest that the PPI–SA mimetic possesses a weak colloidal structure that is severely disrupted by lipid melting[49]. Comparatively, the PPF–SA maintained a higher elastic response even after the lipid phase completely melted, indicating a more intact network resistant to thermal disruption and exhibits greater resistance. Between 40–80°C, although the G' continued to decline, the tan δ gradually decreased to similar levels across all the samples. This indicates a thermal response characterized by a gradual recovery towards elasticity dominated behaviour with similar levels of energy dissipation. The higher G' observed at elevated temperature reflects a more robust network structure within the PPF-SA gel[50]. Upon cooling to 40°C, both G' and tan δ increased due to lipid recrystallization with further cooling the system returned to a state of high G' and total elastic-domination[45]. The superior interfacial stability and thermal stability of the PPF-SA complex enables the construction of a droplet-filled and crosslinked network that replicates the complex thermal response behavior of pork adipose tissue.

2.3.2 Influence of oil-water ratio and Ca^{2+} ionic concentration

The microstructure of the mimetics was investigated by varying the oil/water ratio and Ca^{2+} concentration. As shown in Fig. 4A, at oil/water ratios of 2:8 (2O8H) and 4:6 (4O6H), the mimetics contain small spherical oil droplets uniformly dispersed within the gel matrix network. These oil droplets reduce the porosity of the gel network, and increase available cross-linking sites, thereby driving the formation of a denser and more cohesive three-dimensional network[51]. Consequently, the mimetics retain a high storage modulus (G' >1000 Pa) even at 50–80°C, demonstrating robust thermal stability and an elastic response. In contrast, increasing the oil–water ratio to 60% (6O4H) resulted in larger, irregularly shaped droplets. These droplets impeded effective cross-linking among complexes, reduced cross-link density and disrupted network continuity[52]. As a result, G' fell to 101.2 Pa at 80°C (Fig. 4B), indicating that a high oil/water ratio leads to a decrease in structural integrity and viscoelastic stability, despite the presence of more lipid crystals.

The cross-sectional morphology and thermal stability were evaluated using 3D optical profilometry and temperature sweeps. As shown in Fig. 4C, the mimetics without Ca^{2+} exhibited low peaks and shallow valleys. Increasing the Ca^{2+} concentration yielded taller peaks (red) and deeper valleys (dark blue), indicating a progressive increase in cross-sectional roughness. As shown in Table.1, the R_a value increased significantly from 23.24 ± 2.20 at 0 mM to 80.55 ± 6.70 at 300 mM, while the R_q value increased from 31.29 ± 3.87 to 104.71 ± 10.18. This higher roughness is attributed to the formation of more “egg-box” structures via the cross-linking of G-block in the alginate chains, creating more pronounced structural fluctuations[53]. The thermal stability as a function of Ca^{2+} concentrations was reflected by the gel strength (G') at 80°C. As shown in Fig. 4D, increasing the Ca^{2+} concentration within

the 0–30 mM range did not significantly affect the thermal stability. However, at the 100 mM Ca^{2+} concentration, G' reached 1110 Pa, nearly an order of magnitude higher than at 30 mM, demonstrating a significant improvement in thermal stability. Ca^{2+} cross-linking creates a greater number of junction zones, restricting chain mobility, and droplet coalescence at elevated temperatures[54]. Further increases in Ca^{2+}concentration did not yield additional increases in G', indicating a saturation limit where the fixed number of guluronate units in the alginate chains are fully occupied, preventing further increase in effective junction density[55].

Table 1
R_a (mean roughness) and R_q (root mean square roughness) values of adipose tissue mimetics with different Ca^{2+} concentrations.

Samples	R_a	R_q
0 mM	23.24 ± 2.20^{a}	31.29 ± 3.87^{A}
30 mM	60.21 ± 3.44^{b}	74.87 ± 4.70^{B}
100 mM	74.00 ± 4.53^{bc}	86.26 ± 6.96^{BC}
300 mM	80.55 ± 6.70^{c}	104.71 ± 10.18^{C}

Values are means ± standard deviations of a minimum of three determinations. Mean values in the same column with different superscripts are significantly different.

2.4 Influence of structured lipids on adipose tissue mimetics

2.4.1 Microstructure

The crystalline structure of solid fat can effectively prevent coalescence or aggregation between droplets, thereby improving the stability of adipose tissue mimetics. Here we compare the effects of structured lipids with different MAG contents on the properties of these mimetics. CLSM was used to characterize the distribution of oil droplets (stained with Nile Red) and the proteins (stained with ThT). As shown in Fig. 5A, pork adipose tissue consists of adipocytes approximately 74.12 μm in diameter, which are densely embedded within a network of connective tissue. Upon heating, the fat phase melts, and the tissue softens, while the protein network confers elastic behaviour[56]. The PPI-SA samples lacked a defined lipid droplet structure, instead the lipids were irregularly dispersed throughout the gel matrix, which is consistent with the SEM results. In contrast, the PPF-SA samples consistently exhibited spherical, lipid-encapsulated structures. The overlap of the red (oil droplet) and blue (PPF-SA) fluorescence signals confirms the interfacial adsorption of PPF-SA onto the droplets. This indicates that PPF-SA facilitates the formation of a "lipid-filled structure" similar to natural adipose tissue. PPF tends to accumulate at the interface to prevent droplet aggregation. Moreover, the diameter of these spherical

lipid droplets decreased from 14.50 μm to 5.76 μm as the MAG content increased from 0% to 27% because MAG more effectively reduces the interfacial tension (MacWilliams et al., 2024a). PLM images further illustrate the spatial localization and structural characteristics of the lipids (Fig. 5B). In PPI-SA samples, structured lipids were dispersed in irregular shapes without distinct droplet boundaries. In contrast, in the PPF-SA samples, lipid crystals were primarily localized within spherical droplets.

The Cryo-SEM was used to preserve the original three-dimensional network structure of these mimetics. As shown in Fig. 5C, PPI-SA shows randomly dispersed structured lipids and complexes without distinct droplet structures, consistent with the CLSM observations. By contrast, PPF-SA displayed uniformly distributed droplets filling in a three-dimensional network. In DAG and DAG-8%MAG, densely packed large oil droplets were observed. High-magnification images showed that no continuous gel network formed and only a few interconnected protrusions were present at the oil–water interfaces[57]. This is likely because geometric hindrance and local compression caused by the large droplets limited cross-linking within the continuous phase, leading to aggregation and stacking rather than network percolation. In contrast, MAG content increased from 15% to 27%, a more porous and layered microstructure of gel network and smaller oil droplets were more thoroughly embedded within it. This indicates that the reduced droplet size increased the number of crosslinking sites to enhancing the integrity of the network structure[58]. Similar research indicates that the smaller filling droplets allowed the cross-linked network act as trabecular-like structures, mimicking the extracellular matrix and providing a key structural foundation for an ideal adipose tissue mimetics[43]. The microstructure suggest that these droplets filled with solid lipids mimic the natural structure of pork adipose tissue, allowing the lipids to undergo a phase transition through gradual softening during heating. After that, integrated continuity network provided thermal stability for adipose tissue mimetics.

2.4.2 Melting profiles

As shown in Fig. 5D, pork adipose tissue exhibits a melting peak at 34.06°C, corresponding to the melting of triglycerides[56]. The PPF-SA with DAG sample exhibited the highest melting peak at 49.95°C, while the melting peaks for DAG-8%MAG, DAG-15%MAG and DAG-27%MAG were 41.19°C, 44.08°C and 45.01°C, respectively. Within the emulsion, the lipids were confined within droplets, which impaired molecular mobility, and resulted in a lower solidification temperature compared to the free lipid phase. The melting points of the structured lipids followed the order of MAG > DAG > TAG as higher MAG content promoted the formation of a more robust structured lipid network[59]. This melting behavior is influenced not only by the thermal properties of the lipid components but also by their microscopic distribution within the gel matrix[60]. Consequently, the DAG-8%MAG sample demonstrated a lower melting point due to the combined effects of its lower solid lipid content and smaller droplet size compared to samples containing only DAG[61].

The temperature-sweep results for the adipose tissue mimetics are shown in the Fig. 5E. The G' of all samples decreased between 30–55°C, coinciding with the melting of the structured lipids. This rheological behavior aligns with the DSC results, suggesting that the lipid melting leads to the gradual

softening of the mimetics. Similar studies have shown that without the inclusion of structured lipids, cross-linked mimetic fail to replicate the slow softening (lipid melting) process of animal fat during heating[62]. At 80°C, different thermal stabilities were observed, the G' of the PPF-SA mimetics exhibited an upward trend as the MAG content in the structured lipid increased (Fig. 5E). This is attributed to the higher surface activity of MAG which promoted smaller oil droplets, thereby enhancing cross-linking efficiency and network stability, at high temperatures. Furthermore, after cooling, the structural recovery rate rose from 46.35% to 80.47% with increasing MAG (Fig. 5F). This indicates that larger droplets in DAG-only samples caused void formation after melting, making the network more susceptible to bending and deformation[47]. Consequently, these samples exhibited lower structural recovery rate, only partially restoring their structural strength through lipid recrystallization.

2.4.3 The interfacial properties of complex at the structure lipid surface

To investigate the interfacial properties of the complexes within different structured lipids, the interfacial tension and interfacial dilatational modulus (E_d) were monitored at 65°C, with results depicted in Fig. 6A. The interfacial tension decreased rapidly within 200 s, indicating that the PPF-SA migrated quickly to the oil–water interface. Subsequently, the rate of reduction slowed, suggesting that the complexes underwent reorientation and rearrangement. Notably, increasing the MAG content progressively reduced the equilibrium interfacial tension as the low-molecular-weight emulsifiers continued to migrate toward the interface[63], filling interstitial spaces, and partially replacing the adsorbed PPF-SA[64]. In the DAG-27%MAG system, the PPI-SA exhibited similar adsorption and diffusion trends. However, its interfacial tension increased from 2.96 to 3.57 mN/m (at 3500 s). This rise is attributed to the thermal destabilization of the PPI-SA complex at high temperatures, which reduces its adsorption capacity. Similar studies have reported that thermally destabilized proteins exhibit increased aggregation and impaired interfacial adsorption capacity[65].

The mechanical strength of the interfacial film was evaluated via E_d. As shown in Fig. 6B, E_d increased gradually over time in the DAG system, indicating that PPF-SA progressively adsorbed and formed a viscoelastic film. However, as the MAG content increased to 15%, the growth of the interfacial elastic modulus slowed. In the DAG and DAG-8%MAG, E_d values reached 6.58 and 4,97 mN/m, respectively, whereas in the DAG-15%MAG and DAG-27%MAG, systems, E_d decreased to 1.99 and 2.06 mN/m. These results indicate that MAG can occupy the interface, thereby weakening and partially displacing the elastic film formed by PPF-SA[64]. Interestingly, increasing the MAG concentration to 27% did not further reduce the E_d likely because the high molecular weight and complex three–dimensional structure of the PPF–SA fibrils resisted complete displacement by low–molecular–weight surfactants[66]. In contrast, PPI-SA formed the weakest interfacial film in the presence of DAG-27%MAG. The thermally denatured PPI-SA complex further reduced the film's elastic modulus from 1.43 to 1.26 mN/m, suggesting that an insufficient elastic film is more prone to drainage and rupture eventually leading to droplet coalescence[65].

2.4.4 Water distribution in mimetics with different structured lipids

LF-NMR results reflect water distribution which helps quantify the structural properties of the gel network. In Fig. 6C and Table 2, three water state were observed in all samples: bound water, immobile water, and free water. A small peak at around 0–10 ms (T_{21}) represents bound water which is tightly associated with the carbonyl, amino, and carboxyl groups of the proteins via hydrogen bonding. The dominant peak at approximately 50–150 ms (T_{22}) represents immobilized water retained within the spatial network of the gel. Finally, a weak peak at around 500–2000 ms (T_{23}) indicates free water moving within the network[67]. The results demonstrate that water in mimetics is predominantly composed of bound and restricted water (96.88%), with only a minor free water component (~5 to 6%). This distribution aligns with the inherently low moisture content (5.6%) typically found in adipose tissue, where water is confined within the adipocytes network or bound by the extracellular matrix. This high degree confinement yields shorter T_2 relaxation times and a greater proportion of restricted water[56]. Compared to the PPI-SA emulsions, the PPF-SA sample showed a lower proportion of bound water and a higher proportion of immobilized water. This is likely because the PPF-SA complex forms a denser network structure, the increased cross-linking density shields polar groups and promotes polymer-polymer interactions thereby reducing the available surface sites for hydrogen bonding with water[68].

An in-depth analysis of the water distribution was further conducted using magnetic resonance imaging (MRI). As shown in Fig. 6D, the PPI-SA emulsion exhibited an overall red pseudo-colour. In contrast, the PPF-SA samples maintained high color intensities in the DAG and DAG-8%MAG groups, (maximum intensities of 65534 and 64342, respectively) while a gradual shift toward yellow was observed in the DAG-15%MAG and DAG-27%MAG samples (maximum intensities of 62655 and 61579, respectively). This shift indicates that increased MAG content leads to more tightly bound water. These MRI findings are consistent with the T2 relaxation results, confirming that MAG induced densification of the gel network structure reduces the formation of interconnected water channels[69].

Table 2
Water content, transverse relaxation times, and corresponding proportions of adipose tissue mimetics with different structured lipids.

Samples	Time of Relaxation (ms)			Water Proportions		
	T_{21} (ms)	T_{22} (ms)	T_{23}(ms)	P_{21} (%)	P_{22} (%)	P_{23} (%)
Pork	1.79 ± 0.19^{A}	70.93 ± 7.39^{A}	1335.45 ± 0.00^{A}	2.96 ± 0.11^{ab}	96.88 ± 0.13^{ab}	0.16 ± 0.03^{a}
PPI-SA (DAG-27%MAG)	4.37 ± 0.45^{AB}	144.81 ± 0^{B}	10000 ± 0.00^{B}	2.22 ± 0.10^{ab}	96.91 ± 0.02^{ab}	0.88 ± 0.09^{b}
PPF-SA (DAG)	5.06 ± 0.20^{AB}	155.22 ± 0^{BC}	10000 ± 0.00^{B}	3.42 ± 0.59^{b}	94.35 ± 0.70^{c}	2.23 ± 0.11^{c}
PPF-SA (DAG-8%MAG)	7.50 ± 0.59^{B}	204.91 ± 0^{C}	10000 ± 0.00^{B}	3.70 ± 0.09^{b}	95.24 ± 0.07^{ac}	1.06 ± 0.09^{b}
PPF-SA (DAG-15%MAG)	6.45 ± 5.49^{AB}	270.50 ± 0^{D}	10000 ± 0.00^{B}	2.71 ± 1.73^{b}	96.93 ± 2.00^{ab}	0.36 ± 0.40^{a}
PPF-SA (DAG-27%MAG)	4.05 ± 3.04^{AB}	193.65 ± 0^{BC}	10000 ± 0.00^{B}	1.48 ± 0.74^{a}	97.87 ± 1.25^{b}	0.65 ± 0.52^{ab}

Values are means ± standard deviations of a minimum of three determinations. Mean values in the same column with different superscripts are significantly different.

2.5 Freeze–thawing and thermal stability of adipose tissue mimetics

The internal structure and textural properties of pork adipose tissue are typically influenced by the freeze-thaw process. Freezing induces the formation of ice crystals within the adipose tissue mimetics, which can disrupt the original three-dimensional network structure and lead to textural deterioration. Therefore, the ability of a mimetic to maintain structural integrity and hardness under freeze-thaw conditions is a key indicator for its suitability for application. As shown in Fig. 7A, no apparent water leakage was observed in the adipose tissue mimetics during freeze-thawing. This is because large number of hydrophilic groups in SA interacted with water molecules via hydrogen bonding, inhibiting ice crystals by restricting water mobility and reducing the conversion of bound water to free water[70]. As shown in Fig. 7B, while the hardness of the mimetics was lower than that of natural pork adipose tissue, it remained high attributed to the high-melting point of structured fats and cross-linked SA network.

There was no significant difference in hardness or cohesiveness among samples with different MAG ratios, suggesting a superior ability of the external phase to resist deformation. Furthermore, the springiness of the mimetics prior to freeze-thaw cycles gradually increased with MAG content and was significantly higher than that of pork adipose. Although freeze-thawing caused network disruption by ice crystals leading to a decrease in springiness the value of remained comparable to that of pork adipose. As shown in Table. S1, the gumminess (7, 9, 7 and 6 N) and cohesiveness (0.44, 0.55, 0.56 and 0.53) across different PPF-SA samples were similar to those found in pork (7 N and 0.49, respectively). The high springiness and similar cohesiveness suggest a superior ability to recover internal structure after deformation imparted by the protein-polysaccharide network and lipid crystal droplets. All the samples maintained an intact appearance without structural collapse or oil exudation. However, the significant decrease in springiness and hardness after freeze-thawing treatment (Fig. 7B and Table S2) indicates that the ice crystals weakened the internal network[71]. For PPI-SA sample with 27%MAG, the loose and droplet-free network resulted in lowest hardness (170 N) but acceptable springiness (1.24 mm). In contrast, the PPF-SA sample with 27%MAG, exhibited springiness comparable to pork adipose, indicating that higher MAG content enhances freeze-thaw resistance. The uniform small-droplet structure and denser gel network inhibited the growth of large ice crystals thereby minimized damage to the gel structure[72].

The water-holding capacity (WHC) and oil-holding capacity (OHC) directly influence the greasiness and juiciness of adipose tissue mimetics during cooking. As shown in Fig. 7C, the mimetics maintained their original shape after heating for 30 min, though noticeable leakage of oil and water was observed after 60 min. The PPF-SA samples exhibited a higher OHC values which increased from 79.51% to 92.43% as the MAG content rose from 0.0% to 27.0%. This suggests that the network is more conducive to effectively entrapping oil, thereby reducing the oil migration during heating[10]. The surface-active MAGs promoted the formation of smaller oil droplets, which reduced network pore size, and increased network density, thereby enhancing physical entrapment and water retention[73].

During cooking, pork adipose tissue typically melts partially due to the denaturation of its collagen protein, while the remainder retains its structure to provide chewiness and flavor. For comparison, molded cube gels were heated and photographed to record morphological changes. As shown in Fig. 7D, pork adipose tissue displayed distinct morphologies after 45 min of heating with limited oil loss and only slight structural collapse. In contrast, the PPI-SA gel underwent substantial collapse. This was due to the denaturation and desorption of PPI at high temperatures causing the network to progressively disintegrate, and lead to a marked structural breakdown[74]. On the contrary, the thermal behaviour of the PPF-SA mimetics more closely resembled that of pork adipose tissue, showing limited structural collapse. The PPF-SA stabilized by Ca^{2+} mediated covalent cross-linking, yielding a heat-stable network. During heating, this network preserves the gel matrix and suppresses droplet rupture and migration, effectively simulating the thermal response of natural pork (Wang et al., 2024). Furthermore, the degree of structural collapse gradually decreased with increasing MAG. This is because smaller and uniformly distributed oil droplets within the gel network, act as effective "cross-linking sites" that reinforce the

structure and inhibit collapse [63]. However, samples without a sufficiently rigid network or uniform droplet distribution showed a loss of edges definition and block integrity during heating[75].

2.6 Illustration of the structure stabilization mechanism

Based on the above results, we propose a structural mechanism for the synergistic stabilization provided by the PPF-SA complex and glycerolized PO structured lipids. As shown in Fig. 8, the oil droplets are systematically embedded within a three-dimensional cross-linked network. PPF and SA form a complex through multiple molecular interactions, the exposure of hydrophobic regions and $–NH_3^+$ group in the PPF enhances hydrophobic interactions, electrostatic interaction, and hydrogen bonding with SA. This complex exhibits high interfacial activity and thermal stability, facilitating the construction of a robust droplet-filled structure. Within the PPF-SA composite chains, the $–COO^-$ groups of SA undergo cross-linking with Ca^{2+}, forming the characteristic "$–COO–Ca^{2+}–OOC–$" egg-box structure. This framework establishes an effective physical barrier and a supporting matrix between droplets. Moreover, the DAG and MAG generated from PO glycerolysis optimize the droplet-filling architecture. A higher MAG results in smaller emulsion droplets and a higher crystallization degree, which increases the number of PPF-SA contact sites and reinforces the three-dimensional network. This synergy enhances the structural integrity by constructing a rigid physical network. Consequently, the emulsions exhibit a gradual softening behavior rather than quick collapse under high temperatures and during freeze-thaw cycles.

3. Discussion

This study systematically investigated the use of PPF-SA complexes combined with glycerolized PO structured lipids in the preparation of adipose tissue mimetics. The PPF-SA complex, formed through strong electrostatic, hydrophobic, and hydrogen bond interactions, exhibited superior interfacial activity and enhanced thermal resistance. The resulting adipose tissue mimetics presented a coexistence of droplet packing and a cross-linked network, achieving a storage modulus exceeding 1000 Pa at 80°C. Both the oil/water ratio and Ca^{2+} concentration played a profound regulatory role in the stability of the emulsion gels. Furthermore, increasing the MAG content resulted in smaller droplets and increased water binding capacity. This enhanced the compactness and textural properties under both heating and freeze-thawing treatments, demonstrating high oil and water holding capacities. Therefore, nanoscale protein fibril–SA cross-linking combined with glycerolized lipids can be utilized to design emulsion gel matrices that simulate the thermal-response and freezing-thawing stability of pork adipose tissue. This study provides novel insights and technical strategies for the development of animal fat analogues, particularly, for plant-based meat products whereby fat chunks must remain intact during processing.

4. Materials and methods

4.1 Materials

PO was obtained from Yihai Kerry Co., Ltd, Shanghai, China. Glycerin was purchased from Sigma-Aldrich (Shanghai) Trading Co., (Shanghai, China). Novozyme 435 (Candida antarctica lipase B) was purchased from Novozyme Biotechnology Co., Ltd. (Guangzhou, China). Pea protein (purity > 80.00%) and sodium alginate (SA) were purchased from Shanghai Yuanye Bio-Technology Co., Ltd (Shanghai, China). 1-anilino-8-naphthalenesulfonate magnesium salt (ANS) (purity ≥ 98%), Thioflavin T (Th T), Fluorescein Isothiocyanate (FITC) and Nile Red was purchased from Aladdin Holdings Group Co., Ltd (Beijing China).

4.2 Preparation of pea protein fibrils (PPF) and PPF-SA complex

PPI was fibrillated following an established protocol [76]. Briefly, PPI powder was dissolved in distilled water to obtain a 3 wt% PPI solution. The pH was adjusted to 2 using 6 M HCl, followed by overnight stirring at 4°C. The supernatant was then collected and heated at 85°C for 28 h with constant stirring at 300 rpm. The resulting PPF were collected, cooled in an ice bath, and the pH was adjusted to 7 using 3 M NaOH. SA powder was dissolved in distilled water to obtain a 3 wt% solution. To evaluate the varying roles of protein and the polysaccharide within the complex, the total concentration of PPI/PPF and SA mixture was maintained at 2.6%, with mass ratios of 12:1, 10:3, and 4:9, respectively.

4.3 Characterization of the protein-SA complex

4.3.1 Turbidity, transmission electron microscopy (TEM) and zeta-potential

The complex solution (1 wt%) was diluted 10-fold to measure turbidity (infinite M200 PRO, Tecan Group Ltd., Austria) at 600 nm using a microplate reader. For morphological analysis, the solution was diluted 500-fold and dropped onto a carbon–coated copper grid which was then immersed in phosphotungstic acid (1.0%, w/v) for negative staining. The grid was observed using TEM (1200 EX II, JEOL Inc., Japan) (operating at 120 kV) equipped with a digital camera (FEITecnai–12, Oregon, USA). Additionally, a Zetasizer Nano ZS 90 (Malvern Instruments Co., Ltd., Worcestershire, UK) was used to measure the zeta-potential after diluting the samples 50-fold.

4.3.2 Interfacial properties

The interfacial tension of the complex was measured using the pendant drop method on a video optical contact angle system (OCA-20, Data-Physics Instruments GmbH, Germany) at 25°C. Briefly, a droplet of complex solution (1 wt%) was injected into the purified PO using a syringe (needle diameter of 1.83 mm). The drop profile was recorded, and the interfacial tension was determined by analyzing the shape of the hanging droplet based on the Laplace equation.

To determine the interfacial tension of the complex in various glycerolized lipids the oils were diluted 20-fold with purified PO and heated to 65°C to ensure complete melting. The dynamic interfacial properties were measured by recording the evolution of dilatational parameters using the OCA-20 equipped with an oscillating drop accessory. The deformation amplitude of the drop volume was set at 10%, with an

angular frequency of 0.1 Hz. A 10 µL of droplet was subjected to measurements consisting of five sinusoidal oscillation cycles, interspersed with periods of no oscillation totalling 72 cycles over 60 min. The interfacial elasticity (E_d) was calculated from the resulting interfacial tension data.

4.3.3 Thermal stability

The thermal profile of the complex was determined using a TG/DSC 3 + simultaneous thermal analyzer (Mettler Toledo, Switzerland). Freeze-dried samples (3–5 mg) were heated under an N_2 atmosphere from 30 to 600°C at a constant heating rate of 20 ∘C/min and the change in mass relative to temperature was recorded.

4.3.4 Intrinsic fluorescence and Fourier transform-infrared spectroscopy (FT-IR)

The fluorescence intensity was measured using fluorescence spectrophotometer (F–7000, Hitachi, Japan) with excitation at 280 nm and emission spectra recorded from 290–450 nm at a scan rate of 2400 nm/min. For chemical structure, freeze-dried complexes were ground with KBr and pressed into pellets. FT-IR spectra were recorded in the range of 400 – 4000 cm^{-1} with a resolution of 4 cm^{-1} and 64 scans using a Nicolet iS50 FT-IR spectrometer (Thermo Fisher Scientific Inc., China).

4.3.5 Thioflavin T fluorescence spectroscopy (ThT) and surface hydrophobicity (H_0)

Thioflavin T (8 mg) was dissolved in 10 mL of 10 mM phosphate buffered saline (PBS) containing 150 mM NaCl (pH 7.0) to prepare a ThT stock solution, which was then diluted 50–fold to produce a working solution. A 50 µL aliquot of the 1 wt % complex (diluted 10-fold) was mixed with 4 mL of the ThT working solution and allowed to react for 10 min. H_0 was measured according to previously established methods. Briefly, the complex was diluted and mixed with 8 mM ANS probes (40 µL) for 15 min. The fluorescence intensity was measured using multimode plate reader (infinite M200 PRO, Tecan Group Ltd., Austria) with excitation/emission wavelengths of 440/480 nm for Thioflavin T and 390/470 nm for ANS, respectively. H_0 was calculated based on the slope of the fluorescence intensity plotted against the protein concentration.

4.4 Glycerolysis of PO

The glycerolysis reactions were conducted following a protocol established by previous work (Soleimanian et al., 2024). PO was mixed with glycerol at oil to glycerol molar ratios of 10:3, 10:5 or 10:10. The mixture was stirred at 70°C until completely melted. Distilled water and Novozyme 435 (3 wt % of the substrate) were then added and the glycerolysis reaction was performed under vacuum conditions for 24 h at 70°C. The crude product was purified using a molecular distillation equipment MD III (Foshan Handway Technology Co., Ltd., Foshan, China), with the evaporator temperature set at 190°C, pressure set at 0.1 Pa, and roller speed set at 300 rpm. The resulting structured lipids are designated as

follows: DAG (61.94 ± 0.07%); DAG-8%MAG (DAG: 41.60 ± 0.22%, MAG: 8.59 ± 0.31%); DAG-15%MAG (DAG: 47.15 ± 0.34%, MAG: 14.95 ± 0.07%); DAG-27%MAG (DAG: 45.12 ± 0.90%, MAG: 27.06 ± 0.17%).

4.5 Preparation of adipose tissue mimetics

Emulsion gels were prepared by combining specific proportions of the protein-polysaccharide complexes and structured lipids. Briefly, the lipids were maintained at 65°C to ensure melting, then added to the complex solution (preheated to 65°C) at an oil/water ratio of 4:6. The mixture was homogenized using a high-speed shearing device (Ultra–Turrax IKA–T25, Staufen, Germany) at 10,000 rpm for 2 min while maintaining the temperature at 65°C. The resulting emulsions were cooled at room temperature for 1 h, after which 100 mM $CaCl_2$ solution was added at a $CaCl_2$: gel mass ratio of 1:5. The oil/water volume ratios were varied at 2:8, 4:6, and 6:4 (designated 2O8H, 4O6H, and 6O4H, respectively) with PPF: SA mass ratio fixed at 10:3 (total concentration at 2.6 wt%). To assess the effect of ionic cross linking, the $CaCl_2$ concentration was varied from 0-300 mM using 4:6 oil/water ratio, DAG-27%MAG and a 10:3 PPF: SA ratio. Finally, to assess the effect of different structured lipid types, the DAG, DAG-8%MAG, DAG-15%MAG, DAG-27%MAG were incorporated into mimetics using the 10:3 PPF: SA ratio, 4:6oil/water ratio, and 100 mM $CaCl_2$.

4.6 Characterization of adipose tissue mimetics

4.6.1 Microstructure

Field–emission scanning electron microscopy (FE – SEM) was performed using a Hitachi S – 4800 (Japan) at an accelerating voltage of 5 kV. The mimetics were freeze–dried and cut and mounted onto stubs with double–sided carbon tape and sputter–coated with gold before analysis.

Polarized light microscopy (PLM) was performed using a microscope (Leica DM2700P, Wetzlar, Germany). The cross-section topography of the adipose tissue mimetics was evaluated using a 3D Optical Microscope (Dual Mode 3d Profilometer, Rtec Instruments, San Jose, California, USA) via white light optical interferometry. For this analysis, the freeze–dried mimetics were cut, and placed on glass slides. A 100× objective lens was utilized, and surface data manipulation was performed using Gwyddion (version 2.52, http://gwyddion.net/). For confocal laser scanning light microscopy (CLSM) analysis, the emulsions were stained with Nile Red (0.2 mg/mL in acetone) and ThT (0.2 mg/mL in distilled water). A 20 µL of the stained sample was placed on a slide and allowed to equilibrate for 30 min to ensure acetone evaporation. Images were captured using a Zeiss LSM 880 confocal laser scanning microscope (Carl Zeiss Inc., Oberkochen, Germany). The excitation/emission wavelengths were sets to 520/605 nm for Nile Red and 440/480 nm, for ThT.

Cryo- scanning electron microscopy (Cryo-SEM, S – 4800, Hitachi, Japan). The adipose tissue mimetics were attached to an aluminum sample holder and immersed in a liquid nitrogen. Then, the frozen samples were transferred to a cryo-preparation chamber and disrupted at – 140°C. The fractured

samples were vacuum freeze-drying for 2 h. The sample was observed at a magnification of 400 and 2000 × at an accelerating voltage of 3 kV.

4.6.2 Melting behavior and temperature sweep tests

The melting behavior of mimetics was measured using a DSC instrument (DSC1 500 instrument, Mettler Toledo, Zurich, Switzerland). Samples (8–12 mg) were hermetically sealed in an aluminum pan (5 mL) with an empty pan used as a reference. The samples were heated from 4 to 90°C at a constant rate of 5°C min^{-1}.

Temperature sweep tests were performed using a Thermo Scientific HAAKE Rotation Rheometer Typ006–1659 (Karisruhe, Germany) equipped with a circulating water temperature control system and a cross–hatched parallel geometry (diameter 25 mm, a gap 1.0 mm). The temperature program consisted of heating from 4°C to 80°C at 5°C/min, holding at 80°C for 1 min, and then cooling from 80°C to 4°C at 5°C/min. All measurements were conducted at a strain amplitude of 0.01% and a frequency of 0.1 Hz. The structural recovery percentage was calculated by comparing the average G' value after cooling to the initial value before heating. The tan δ was calculated as ratio of loss modulus G" to the storage G'.

4.6.3 Water distribution and freeze-thaw stability

The water distribution within mimetics was determined using a pulsed nuclear magnetic resonance (p-NMR) spectrometer (NM-2, Shanghai Niumai Electronic Technology Co. Ltd., China). For the freeze-thawing assessment: freshly prepared adipose tissue mimetics were stored at − 20°C for 24 h and then thawed at 25°C for 2 h. This process was repeated for 2 cycles. A TA-XT Plus texture analyzer (Stable Microsystems, Surrey, UK) was used to measure the hardness of the samples before and after freeze-thaw treatment. A TA10 probe was employed for compression tests, with the pre-test, test, and post-test speeds all set at 1.0 mm/s and a compression distance of 7 mm. Data were analyzed using Texture Exponent software v.6.1.1.0. The peak force (g) was defined as the hardness.

4.6.4 Heat stability and meltability

The mimetics were heated at 100°C for 30 minutes, then centrifuged at 3000 rpm for 5 min at 25°C. Any leaked moisture was absorbed using filter paper prior to weighing. Water holding capacity (WHC) and oil holding capacities (OHC) were calculated by comparing the moisture and lipid content pre- and post-centrifugation. Additionally, to simulate cooking conditions, samples were heated at 160°C for 45 min in a convection oven (DKX-R40S6, Bar, China) at 160°C.

4.7 Statistical analysis

Data were analyzed using one–way analysis of variance (ANOVA) with the least significant difference test applied at significant threshold of $p < 0.05$. Statistical analyses were conducted using Origin 8.5 and SPSS 13.0 software (SPSS Inc., Chicago, USA). All measurements were performed in triplicate and the results are expressed as the mean ± standard deviation.

Declarations

Data availability

Data will be made available on request.

Acknowledgments

Financial support from National Key Research and Development Program of China (2024YFE0214900), National Natural Science Foundation of China (32572478), Key R&D Program of Shandong Province, China (2024CXGC010914), the Guangdong Basic and Applied Basic Research Foundation (2024A1515011733, 2025A1515012832) are acknowledged.

Author contributions

B.J.H: Conceptalization, Data Curation & Analysis, Methodology, Writing-Original Draft, Writing-Review & Editing. K. D: Data Curation, Methodology. Y.Y.L: Writing- original draft. H.L：Conceptalization, Data Curation. C.P.T: Conceptualization. M.Z: Data curation, Methodology. C.Y.Q and Y.W: Conceptualization, Formal analysis, Funding acquisition, Project administration, Supervision, Writing-Review &Editing, Funding acquisition.

Competing interests

The authors declare no competing interests.

Additional information

Correspondence and requests for materials should be addressed to Chaoying Qiu.

References

1. Lee, M. et al. Cultured meat with enriched organoleptic properties by regulating cell differentiation. *Nat Commun* 15, 77 (2024).
2. Wood, J. D., Giromini, C. & Givens, D. I. Animal-derived foods: consumption, composition and effects on health and the environment: an overview. *Front. Anim. Sci.* 5, 1332694 (2024).
3. Nicholson, R. A. & Marangoni, A. G. Glycerolysis structured oils as natural fat replacements. *Current Opinion in Food Science* 43, 1–6 (2022).
4. Nicholson, R. A. & Marangoni, A. G. Lipase-catalyzed glycerolysis extended to the conversion of a variety of edible oils into structural fats. *Current Research in Food Science* 4, 163–174 (2021).
5. Xie, P. et al. Interactions between proteins and partial acylglycerols at oil-water and air-water interfaces of partially crystalline emulsions: Interfacial structure, adsorption, and foaming behavior. *Food Hydrocolloids* 172, 112157 (2026).

6. Gulzar, S., Hosseini, A. F., Martín-Belloso, O., Soliva-Fortuny, R. & Rizvi, S. S. H. Engineering Processes for Plant-Based Meat Analogs: Current Status and Future Outlook. *Comp Rev Food Sci Food Safe* 24, e70322 (2025).
7. Wang, Y. et al. Emulsion gels of oil encapsulated in double polysaccharide networks as animal fat analogues. *Food Hydrocolloids* 171, 111807 (2026).
8. Teng, C. & Campanella, O. H. A Plant-Based Animal Fat Analog Produced by an Emulsion Gel of Alginate and Pea Protein. *Gels* 9, 393 (2023).
9. Czapalay, E. & Marangoni, A. Functional properties of oleogels and emulsion gels as adipose tissue mimetics. *Trends in Food Science & Technology* 153, 104753 (2024).
10. Huang, S. et al. Pectin based gels and their advanced application in food: From hydrogel to emulsion gel. *Food Hydrocolloids* 160, 110841 (2025).
11. Kamlow, M.-A., Spyropoulos, F. & Mills, T. 3D printing of kappa-carrageenan emulsion gels. *Food Hydrocolloids for Health* 1, 100044 (2021).
12. Jiang, R. et al. Formation Mechanism and Morphology Control of Glutenin Microtubes Prepared Using Acid-Heat Treatment. *J. Agric. Food Chem.* 73, 31573–31589 (2025).
13. Ouyang, K. et al. Whey protein isolate nanofibrils formed with phosphoric acid: Formation, structural characteristics, and emulsion stability. *Food Hydrocolloids* 135, 108170 (2023).
14. Chen, S., Wei, M., Liu, G. & Liu, B. Construction and Characterization of Emulsions Stabilized by Whey Protein Isolate-Naringin-Sodium Alginate Ternary Complex. *Foods* 15, 19 (2025).
15. Wei, Z. et al. Soy Protein Amyloid Fibril Scaffold for Cultivated Meat Application. *ACS Appl. Mater. Interfaces* 15, 15108–15119 (2023).
16. Zhu, Q. et al. Encapsulation of lycopene in Pickering emulsion stabilized by complexes of whey protein isolate fibrils and sodium alginate: Physicochemical property, structural characterization and in vitro digestion property. *Food Research International* 191, 114675 (2024).
17. Wang, Q. et al. Sanxan–Protein Complex Particles for Stabilization of Pickering Emulsions: Improving Emulsification Properties. *Foods* 13, 3854 (2024).
18. Sun, J., Yang, X., Diao, J., Wang, Y. & Wang, C. Exploration of Pea Protein Isolate–Sodium Alginate Complexes as a Novel Strategy to Substitute Sugar in Plant Cream: Synergistic Interactions Between the Two at the Interface. *Foods* 14, 991 (2025).
19. Jiang, F. et al. Tunable self-assemblies of whey protein isolate fibrils for pickering emulsions structure regulation. *Food Hydrocolloids* 124, 107264 (2022).
20. Zhou, Q., Xu, Z. & Wei, Z. Precise control of aggregation morphology: Effective strategy to tune the properties of ovotransferrin particles. *International Journal of Biological Macromolecules* 253, 126850 (2023).
21. Babu, A., Shams, R., Dash, K. K., Shaikh, A. M. & Kovács, B. Protein-polysaccharide complexes and conjugates: Structural modifications and interactions under diverse treatments. *Journal of Agriculture and Food Research* 18, 101510 (2024).

22. Feng, J. et al. Combining different ionic polysaccharides and pH treatment improved functional properties of soybean protein amyloid fibrils through structural modifications. *Food Hydrocolloids* 153, 110027 (2024).
23. Chen, Y. et al. Interfacial behavior and emulsifying properties of coconut protein glycated by polygalacturonic acid with different molecular weight. *International Journal of Biological Macromolecules* 298, 139825 (2025).
24. Shi, Y., Cao, J., Li, L. & Yang, X. Enhancing stability and performance of emulsion stabilized by soy protein isolate nanofiber - polysaccharide complexes. *LWT* 205, 116495 (2024).
25. Zhang, Z. *et al.* Preparation, properties and interaction of curcumin loaded zein/HP-β-CD nanoparticles based on electrostatic interactions by antisolvent co-precipitation. *Food Chemistry* 403, 134344 (2023).
26. Wang, M. et al. Effect of honeysuckle leaf extract on the physicochemical properties of carboxymethyl konjac glucomannan/konjac glucomannan/gelatin composite edible film. *Food Chemistry: X* 18, 100675 (2023).
27. Xu, M. et al. Complex coacervation of soy protein isolate-limited enzymatic hydrolysates and sodium alginate: Formation mechanism and its application. *Food Science & Nutrition* 10, 4178–4188 (2022).
28. Liu, Y. et al. Application of cod protein-stabilized and casein-stabilized high internal phase emulsions as novel fat substitutes in fish cake. *LWT* 173, 114267 (2023).
29. Li, T. et al. Sodium alginate-mediated interfacial structuring in soy protein-quercetin composite emulsions: A synergistic strategy for encapsulation and bioavailability enhancement of lipophilic bioactives. *Food Chemistry* 493, 145812 (2025).
30. Xi, C., Sun, Z., Chen, X., Ding, X. & Zhang, T. Characterization of coacervation behavior between whey protein isolate and propylene glycol alginate: A morphology, spectroscopy, and thermodynamics study. *Food Chemistry: X* 15, 100402 (2022).
31. Nishinami, S., Arakawa, T. & Shiraki, K. Classification of protein solubilizing solutes by fluorescence assay. *International Journal of Biological Macromolecules* 203, 695–702 (2022).
32. Yu, Z. et al. Formation, structure and functional characteristics of amyloid fibrils formed based on soy protein isolates. *International Journal of Biological Macromolecules* 254, 127956 (2024).
33. Kutzli, I. et al. From amyloid fibrils to microfiber condensates: Tuning microfluidic coextrusion of food-grade β-lactoglobulin-pectin core-shell fibers by changes of protein structure. *Food Hydrocolloids* 143, 108845 (2023).
34. Yoon, W. B., Jung, H. & Oyinloye, T. M. Synergistic Effects of Pea Protein on the Viscoelastic Properties of Sodium Alginate Gels: Findings from Fourier Transform Infrared and Large-Amplitude Oscillatory Shear Analysis. *Processes* 12, 1638 (2024).
35. Savić Gajić, I. M., Savić, I. M. & Svirčev, Z. Preparation and Characterization of Alginate Hydrogels with High Water-Retaining Capacity. *Polymers* 15, 2592 (2023).
36. Feng, Q. et al. Rhizobacteria protective hydrogel to promote plant growth and adaption to acidic soil. *Nat Commun* 16, 1684 (2025).

37. Liu, C. et al. Study on the formation mechanism of pea protein nanofibrils and the changes of structural properties of fibril under different pH and temperature. *Food Hydrocolloids* 150, 109735 (2024).
38. Yang, Q., Yu, X.-H., Zhang, J.-W., Jiang, Y.-X. & Chen, H.-Q. The complex of arachin amyloid-like fibrils formed with ultrasound treatment and chitosan: A potential vehicle for betanin and curcumin with improved chemical stability and slow release in vitro. *Food Hydrocolloids* 166, 111272 (2025).
39. Khalesi, H. et al. Influence of amyloid fibril length and ionic strength on WPI-based fiber-hydrogel composites: Microstructural, rheological and water holding properties. *Food Hydrocolloids* 148, 109499 (2024).
40. Miao, L. et al. Effects of fibrillation combined with glycation by different chain length sugars on structural and functional properties of soybean protein. *Food Hydrocolloids* 153, 110026 (2024).
41. Wang, X. et al. Fabrication and Characterization of Gel Beads of Whey Isolate Protein–Pectin Complex for Loading Quercetin and Their Digestion Release. *Gels* 8, 18 (2021).
42. Yao, X. et al. Solvent-adaptive hydrogels with lamellar confinement cellular structure for programmable multimodal locomotion. *Nat Commun* 15, 9254 (2024).
43. Zhang, T. et al. Dual network interpenetration emulsion gels based on alginate and coffee cherry-derived polysaccharides: preparation, characterization, and curcumin delivery. *Food Chemistry* 494, 146186 (2025).
44. Lorenzen, M., Van Den Berg, F. W. J., Lillevang, S. K. & Ahrné, L. The effect of milk fat content on microstructure and rheological properties of rennet casein gel emulsions. *Food Hydrocolloids* 146, 109243 (2024).
45. Wijarnprecha, K. et al. Temperature-dependent properties of fat in adipose tissue from pork, beef and lamb. Part 2: rheology and texture. *Food Funct.* 13, 7132–7143 (2022).
46. Wei, W., Cui, L. & Meng, Z. The potential of protein-polysaccharide-based O/W and W/O emulsion gels strengthened by solid fat crystallization as realistic fat analogs. *Food Chemistry* 464, 141889 (2025).
47. Choi, M., Choi, H. W., Kim, H. E., Hahn, J. & Choi, Y. J. ate. *Food Hydrocolloids* 145, 109043 (2023).
48. Li, A., Gong, T., Hou, Y., Yang, X. & Guo, Y. Alginate-stabilized thixotropic emulsion gels and their applications in fabrication of low-fat mayonnaise alternatives. *International Journal of Biological Macromolecules* 146, 821–831 (2020).
49. Wang, Z., Chandrapala, J., Truong, T. & Farahnaky, A. Multicomponent Oleogels Prepared with High- and Low-Molecular-Weight Oleogelators: Ethylcellulose and Waxes. *Foods* 12, 3093 (2023).
50. Santamaría, E., Maestro, A., Chowdhury, S., Vílchez, S. & González, C. Rheological study of pullulan-pectin mixtures to prepare gel beads using the drip method and evaluation as gallic acid release systems. *Food Hydrocolloids* 160, 110747 (2025).
51. Li, S., Chen, G., Shi, X., Ma, C. & Liu, F. Comparative Study of Heat- and Enzyme-Induced Emulsion Gels Formed by Gelatin and Whey Protein Isolate: Physical Properties and Formation Mechanism. *Gels* 8, 212 (2022).

52. Su, C., Li, D., Wang, L. & Wang, Y. *Food Hydrocolloids* 157, 110439 (2024).
53. Wang, H., Yang, L. & Yang, Y. A review of sodium alginate-based hydrogels: Structure, mechanisms, applications, and perspectives. *International Journal of Biological Macromolecules* 292, 139151 (2025).
54. Wang, Y. et al. Progress in Research on Metal Ion Crosslinking Alginate-Based Gels. *Gels* 11, 16 (2024).
55. Malektaj, H., Drozdov, A. D. & deClaville Christiansen, J. Mechanical Properties of Alginate Hydrogels Cross-Linked with Multivalent Cations. *Polymers* 15, 3012 (2023).
56. Wijarnprecha, K. et al. Temperature-dependent properties of fat in adipose tissue from pork, beef and lamb. Part 1: microstructural, thermal, and spectroscopic characterisation. *Food Funct.* 13, 7112–7122 (2022).
57. Zhang, B., Mai, H., Liang, X., Liu, Y. & Huang, W. g emulsion gels with enhanced physical stability. *Food Hydrocolloids* 166, 111336 (2025).
58. Choi, M., Choi, H. W., Choe, Y., Hahn, J. & Choi, Y. J. Development of emulsion gels as animal fat analogs: The impact of soybean and coconut oil concentration on rheological and microstructural properties. *Food Chemistry: X* 27, 102439 (2025).
59. Nicholson, R. A. & Marangoni, A. G. Lipase-catalyzed glycerolysis extended to the conversion of a variety of edible oils into structural fats. *Current Research in Food Science* 4, 163–174 (2021).
60. Kupikowska-Stobba, B., Domagała, J. & Kasprzak, M. M. Critical Review of Techniques for Food Emulsion Characterization. *Applied Sciences* 14, 1069 (2024).
61. Chen, L. & Doyle, P. S. Design and Use of a Thermogelling Methylcellulose Nanoemulsion to Formulate Nanocrystalline Oral Dosage Forms. *Advanced Materials* 33, 2008618 (2021).
62. Ye, X. et al. Modulation of double network assembly via different calcium sources and GDL concentrations for simulating intramuscular fat. *npj Sci Food* 9, 286 (2025).
63. MacWilliams, S. V., Clulow, A. J., Gillies, G., Beattie, D. A. & Krasowska, M. Recent advances in studying crystallisation of mono- and di-glycerides at oil-water interfaces. *Advances in Colloid and Interface Science* 326, 103138 (2024).
64. Chen, W. et al. Impact of soy proteins, hydrolysates and monoglycerides at the oil/water interface in emulsions on interfacial properties and emulsion stability. *Colloids and Surfaces B: Biointerfaces* 177, 550–558 (2019).
65. Ma, J. et al. Effects of protein concentration, ionic strength, and heat treatment on the interfacial and emulsifying properties of coconut (Cocos nucifera L.) globulins. *Food Chemistry: X* 20, 100984 (2023).
66. Wang, Z. et al. Physicochemical Quantitative Analysis of the Oil–Water Interface as Affected by the Mutual Interactions between Pea Protein Isolate and Mono- and Diglycerides. *Foods* 13, 176 (2024).
67. Zhao, D. et al. Effect of palm oil content and melting point on the freeze-thaw stability of fat substitutes. *LWT* 188, 115452 (2023).

68. Huang, J. et al. Effect of phosphates on gelling characteristics and water mobility of myofibrillar protein from grass carp (Ctenopharyngodon idellus). *Food Chemistry* 272, 84–92 (2019).
69. Wang, Z. et al. Investigating Texture and Freeze–Thaw Stability of Cold-Set Gel Prepared by Soy Protein Isolate and Carrageenan Compounding. *Gels* 10, 204 (2024).
70. Guan, H. et al. Effect of sodium alginate on freeze-thaw stability of deacetylated konjac glucomannan gel. *Journal of Food Engineering* 383, 112239 (2024).
71. Jiang, X., Liang, Q. & Shi, W. Influence of starch on freeze-thaw stability of Hypophthalmichthys molitrix surimi gel observed via ice crystal distribution and gel properties. *Food Chemistry: X* 24, 101995 (2024).
72. Yu, J., Wang, Y., Li, D. & Wang, L. Freeze-thaw stability and rheological properties of soy protein isolate emulsion gels induced by NaCl. *Food Hydrocolloids* 123, 107113 (2022).
73. Zeng, L., Lee, J., Jo, Y.-J. & Choi, M.-J. Effects of micro- and nano-sized emulsions on physicochemical properties of emulsion–gelatin composite gels. *Food Hydrocolloids* 139, 108537 (2023).
74. Yang, J. et al. The impact of heating and freeze or spray drying on the interface and foam stabilising properties of pea protein extracts: Explained by aggregation and protein composition. *Food Hydrocolloids* 133, 107913 (2022).
75. Wen, Y., Che, Q. T., Kim, H. W. & Park, H. J. Potato starch altered the rheological, printing, and melting properties of 3D-printable fat analogs based on inulin emulsion-filled gels. *Carbohydrate Polymers* 269, 118285 (2021).
76. Hu, B. et al. Modulating mechanisms of pea protein fibrils on the interfacial distribution of diacylglycerol and structural rigidity of emulsion gel. *Food Hydrocolloids* 172, 112152 (2026).

Figures

Figures

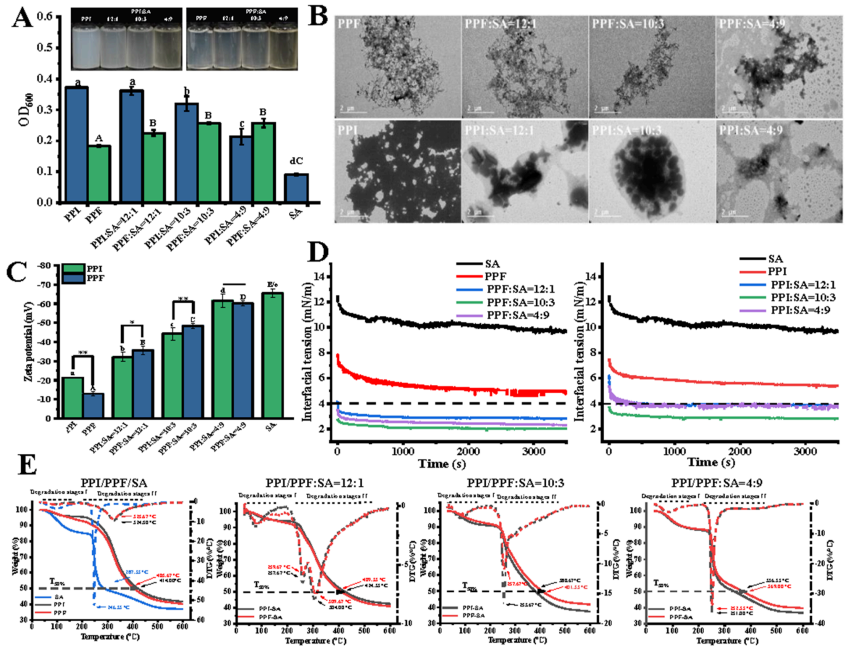


Fig. 1. The visual appearance, turbidity (OD600) (A) and TEM images (B) of PPI-SA and PPF-SA with different mass ratios at 12:1,10:3 and 4:9 (w/w). The scale bar is 2 μm. The zeta-potential (C), interfacial tension (D), thermogravimetric (TGA) and differential thermal gravimetric (DTG) (E) analysis of PPI-SA and PPF-SA with different mass ratios at 12:1, 10:3 and 4:9 (w/w). The total mass of the complex is 2.60 wt%. Different superscript letters indicated significant differences ($p < 0.05$).

Figure 1

See image above for figure legend.

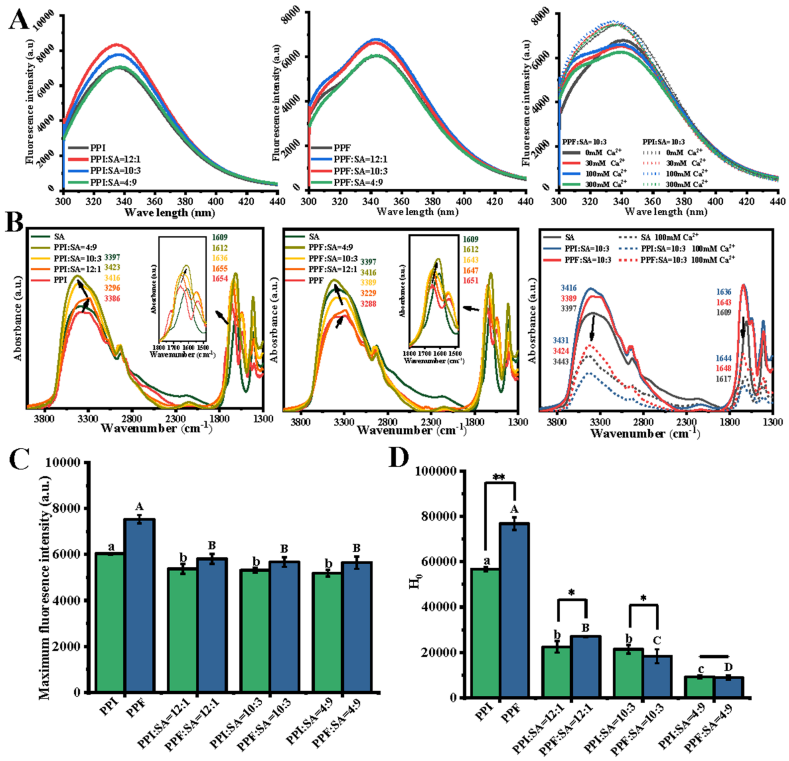


Fig. 2. The intrinsic fluorescence spectra (A) and FTIR (B) of PPI-SA and PPF-SA with different mass ratios. PPI-SA and PPF-SA at mass ratios 10:3 with different Ca^{2+} concentrations 0, 30, 100 and 300mM.The maximum ThT fluorescence intensity (C) and surface hydrophobicity (D) of PPI-SA and PPF-SA with different mass ratios. Different superscript letters indicated significant differences ($p < 0.05$).

Figure 2

See image above for figure legend.

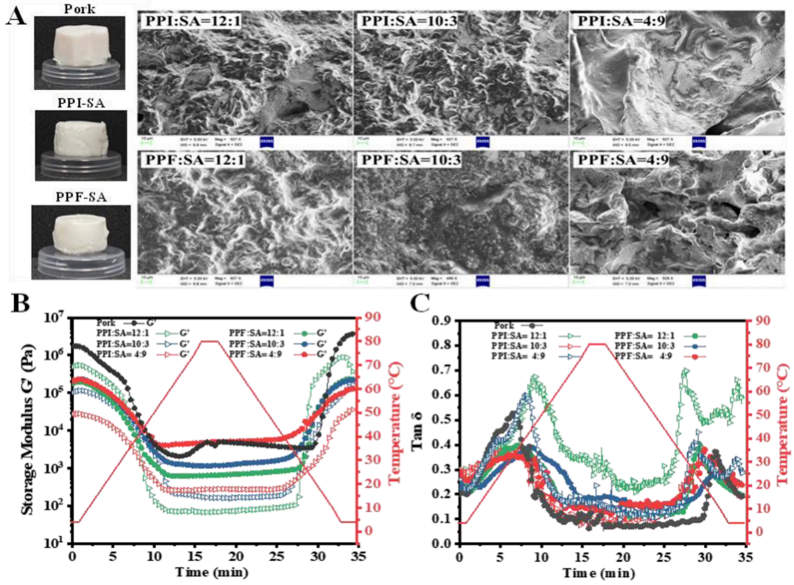


Fig. 3. The visual appearance (A) and SEM images (B) of adipose tissue mimetics with PPI-SA and PPF-SA with different mass ratios (12:1, 10:3 and 4:9) and lipid of DAG-27%MAG. Temperature sweeps (A) and tan δ (B) of adipose tissue mimetics with PPI-SA and PPF-SA with different mass ratios at 12:1,10:3 and 4:9. The red line represents temperature variation over time (G′ and G″ are shown as filled and open symbols, respectively).

Figure 3

See image above for figure legend.

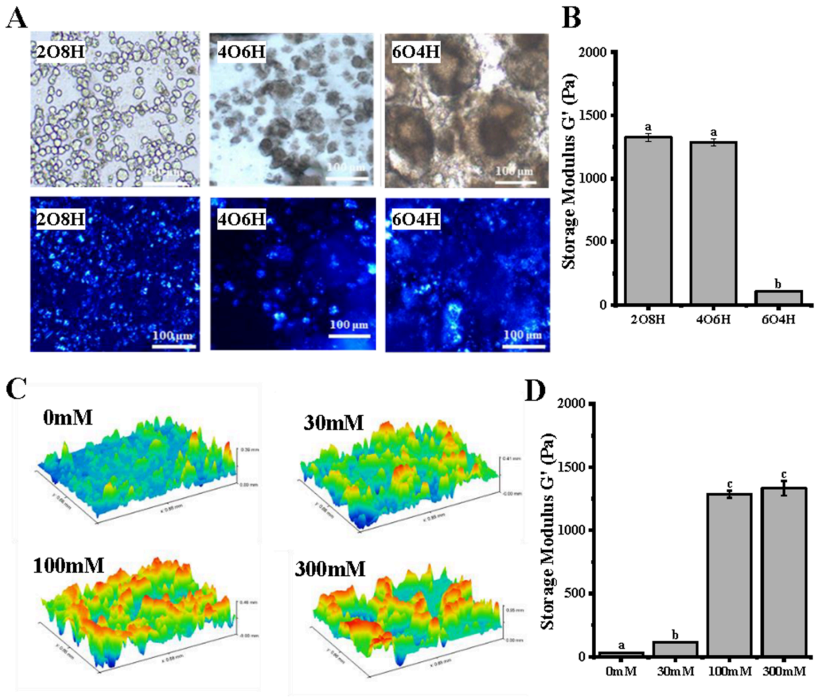


Fig. 4. PLM (A) and gel strength (G') (B) of adipose tissue mimetics of PPF-SA at mass ratios 10:3 with different oil-water ratios at 2:8 (2O8H), 4:6 (4O6H), and 6:4 (6O4H). 3D surface profile (C) and gel strength (G') (D) of adipose tissue mimetics of PPF-SA at mass ratios 10:3 with different Ca^{2+} concentrations 0, 30, 100 and 300mM. The G' is derived from the average value of the temperature sweeps at 80 °C. Different superscript letters indicated significant differences ($p < 0.05$).

Figure 4

See image above for figure legend.

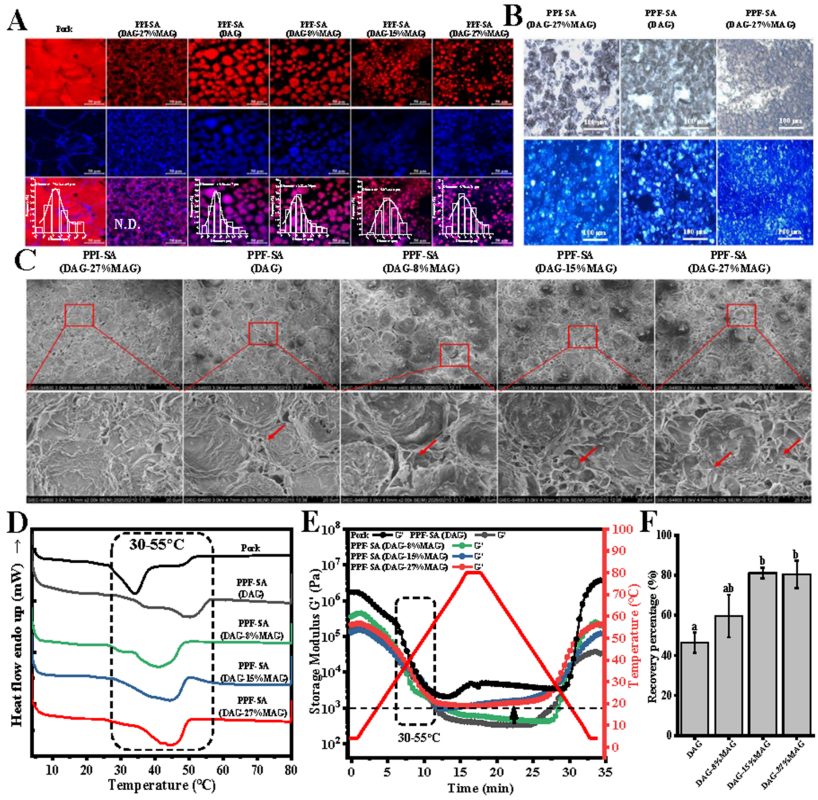


Fig. 5. CLSM (A), PLM (B) and Cryo-SEM images (C) of adipose tissue mimetics with different structured PPF-SA at mass ratios 10:3 and Ca^{2+} 100mM. DSC (D), temperature sweeps (E) and recovery percentage (%) (F) of adipose tissue mimetics with different structured lipids PPF-SA at mass ratios 10:3 and Ca^{2+} 100mM. The red line represents temperature variation over time. Different superscript letters indicated significant differences ($p < 0.05$).

Figure 5

See image above for figure legend.

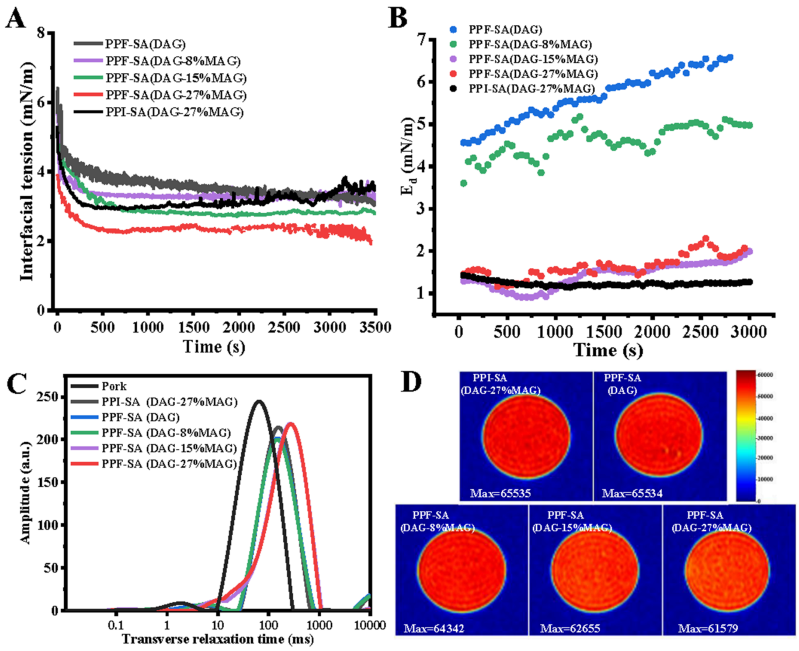


Fig. 6. The interfacial tension (A) and interfacial dilatational modulus (E_d) (B) of PPF-SA with different structured lipids. The plotting of the curve of transverse relaxation time(C) and magnetic resonance images (D) of adipose tissue mimetics with different structured lipids.

Figure 6

See image above for figure legend.

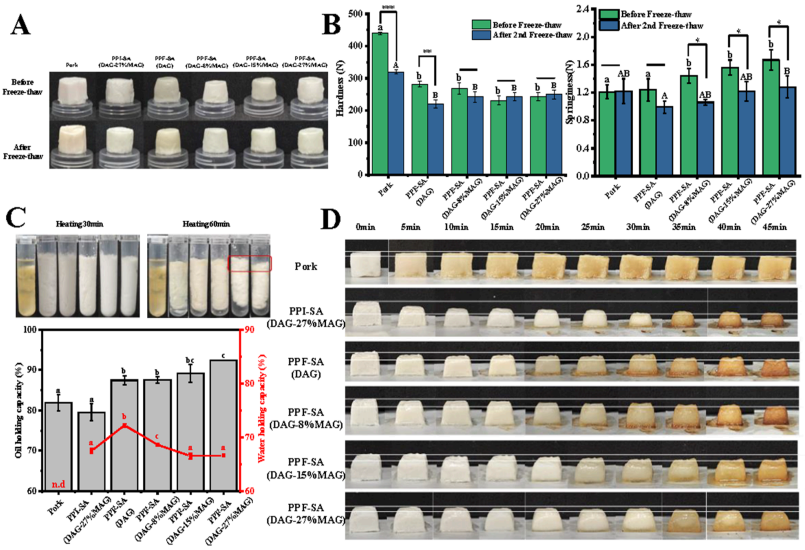


Fig. 7. The visual appearance (A) and texture profile analysis (B) of adipose tissue mimetics with different structured lipids before and after 2-nd freeze-thaw. Heating stability (C) and cooking morphological changes (C) of adipose tissue mimetics with different structured lipids. Different superscript letters indicated significant differences ($p < 0.05$). The heating stability and meltability of adipose tissue mimetics with different structured lipids.

Figure 7

See image above for figure legend.

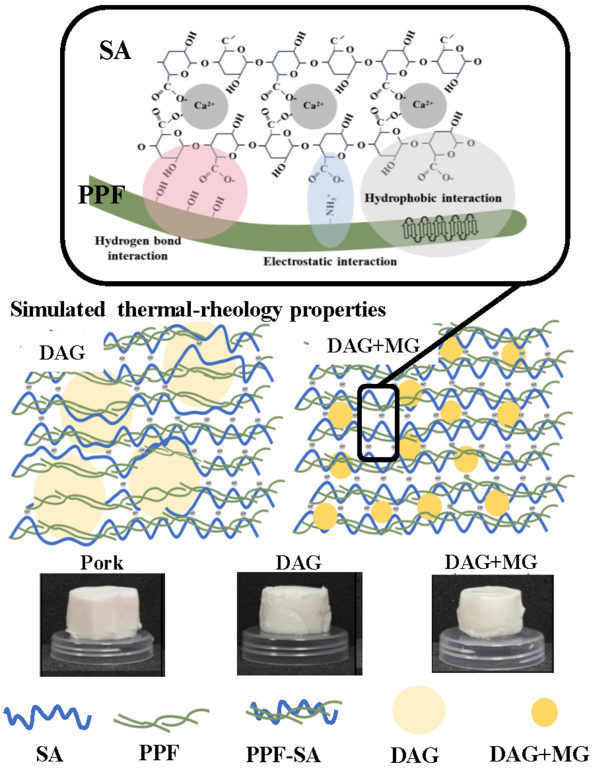


Fig. 8. Schematic illustration of PPF-SA interaction and structure stabilization mechanism of adipose tissue mimetics.

Figure 8

See image above for figure legend.

Supplementary Files

This is a list of supplementary files associated with this preprint. Click to download.

- Supplementarymaterial20260213.docx